Pergamon

Int. J. Heat Mass Transfer. Vol. 40, No. 4, pp. 823–842, 1997

0017-9310/97 $17.00 + 0.00

PII: S0017-9310(96)00151-2

Variable density effects in axisymmetric isothermal turbulent jets: a comparison between a first- and a second-order turbulence model

J. P. H. SANDERS, B. SARH and I. GÖKALP

Laboratoire de Combustion et Systèmes Réactifs, Centre National de la Recherche Scientifique, 1C Avenue de la Recherche Scientifique, 45071 Orléans Cedex 2, France

(*Received* 31 *January* 1995 *and in final form* 25 *April* 1996)

Abstract—The standard k–ε model and a second-order Reynolds stress model (RSM) are used to investigate variable density effects in axisymmetric turbulent jets. Without buoyancy, both models predict no effect of the varying density on the far field turbulence parameters and the classical effective diameter concept works for the decay rates. No conclusive disagreement with experimental data is observed. Effects of turbulence production due to buoyancy are found to be small compared to the effect of the mean buoyancy term in the momentum equation. However, this turbulence production has a large influence on the axial scalar flux, for which the experimental trend is predicted with the second-order model but not at all with the k–ε model. Copyright © 1996 Elsevier Science Ltd.

1. INTRODUCTION

Variable density effects play an important role in many applications, notably where mixing of gases in combustion processes is involved. The present study concentrates on the behaviour of variable density isothermal jets. The variable density effects considered here are therefore generated by the mixing of two gases of different density. The strength of these effects can be characterized by the initial density ratio $\omega = \rho_a/\rho_j$ of the ambient density and the density of the jet fluid. Since vertical variable density jets usually are subject to gravitional acceleration, it is useful to know when buoyancy effects are important. These effects can be quantified by the (densimetric) Froude number

$$Fr = \frac{\rho_j U_j^2}{gD|\rho_a - \rho_j|} = \frac{U_j^2}{gD|1-\omega|} \tag{1}$$

where U_j is the mean jet exit velocity. If Fr is very large, buoyancy effects will become important only at very large axial distances. For pure jets (either $\omega = 1$ or $g = 0$), Fr is infinite. Three different regions can be observed in turbulent buoyant jets: a convection dominated region close to the nozzle (if the Froude number is sufficiently large), a buoyant intermediate region, and in the far field the flow becomes a buoyant plume. At very low Froude numbers the plume region begins already close to the nozzle, while at high Froude numbers it begins far downstream. Chen and Rodi [1] define a scaled distance $\hat{x} = Fr^{-1/2}(\rho_j/\rho_a)^{-1/4}x/D$. Based on experimental results, they find that buoyancy becomes important at $\hat{x} \approx 0.5$, so at an axial distance $x_b/D \approx Fr^{1/2}(\rho_j/\rho_a)^{1/4}\hat{x}$.

Variable density effects can be classified in two main categories. The first is related to global effects on the mean velocity, mixture fraction or turbulence quantities, which can directly be explained by concepts like the conservation of mass and momentum. For instance, the concept of conservation of momentum is the basis for the introduction of an effective jet diameter by which the decay of the centreline mean velocity and the mean mixture fraction for all ω would 'collapse' onto a single curve [1, 2] for pure jets, i.e. non-buoyant jets. The second category of variable density effects is related to more 'subtle' effects that cannot be directly explained with these concepts and possibly involve additional mechanisms such as the role of correlations between density fluctuations and velocity fluctuations [3, 4] or effects related to turbulence production due to buoyancy. There is no real consensus in the experimental literature regarding these effects. For instance, changes in the velocity spreading rates as a function of ω are observed in several experimental studies [5–7]. However, there is also experimental literature in which this is not observed [8–10], where the latter reference only considers the mixture fraction (scalar) spreading rate. Another example of a subtle effect is an increase with ω of second-order turbulence correlations involving the axial velocity fluctuation [7].

In the present study, the characteristics of variable density axisymmetric isothermal vertical turbulent jets

NOMENCLATURE

$\mathbf{b}_{ij}$ anisotropy tensor
C coefficients
D nozzle diameter, diffusion term or coefficient
f mixture fraction
$\widetilde{f''^2}$ scalar variance
F mean mixture fraction
Fr Froude number
g_i gravitational acceleration in direction i
G production term due to buoyancy
k turbulent kinetic energy
K_u, K_f velocity and scalar decay rates
K'_u, K'_f normalized velocity and scalar decay rates
L_u, L_f velocity and scalar halfwidth
p pressure
P production term
r radial distance
Re Reynolds number
Re_t turbulent Reynolds number
S_u, S_f spreading rates
Sc_t turbulent Schmidt number
u axial velocity
U mean axial velocity
U_i mean velocity in direction i
v radial velocity
V mean radial velocity
w tangential velocity
x axial distance
x_b buoyant axial distance.

Greek symbols
α turbulence coefficient
β_e expansion coefficient
δ_{ij} Kronecker delta
ε dissipation rate of turbulent energy
ε_f scalar dissipation rate
ϕ generalized variable
ω density ratio ($=\rho_a/\rho_j$)
ν molecular kinematic viscosity
ρ density
σ turbulent Prandtl number
θ azimuthal angle.

Subscripts
a ambient fluid
c centreline
cofl coflow
eff effective
f scalar transport
j jet fluid
i, j, k directional index.

Superscripts
$\tilde{\phi}$ Favre average of ϕ
$\bar{\phi}$ Conventional average of ϕ
$''$ Favre fluctuation
$'$ Conventional fluctuation.

are predicted with a first- and a second-order turbulence model. Both pure jets and buoyant jets are studied for density ratios of $0.25 < \omega < 20$. These predictions are compared with each other and with available experimental data. The goal of the study is to investigate the differences between the two turbulence models in the prediction of this type of flow and to investigate which effects, that are experimentally established, can and cannot be predicted by these models.

2. GOVERNING EQUATIONS

In the conservation equations, mass-weighted averaging is applied to avoid the appearance of many terms involving density fluctuations for which additional models are needed. A mass averaged quantity is defined as

$$\tilde{\phi} = \frac{\overline{\rho\phi}}{\bar{\rho}}. \tag{2}$$

The mean tangential velocity W is zero in the present configuration. However, in the instantaneous momentum equations, quadratic terms of w are not suppressed because they lead to the normal stress $\widetilde{w''w''}$ (the overbar denotes the range of the tilde) which is not zero. This would be the case in two-dimensional turbulence, but here three-dimensional turbulence is considered. The axisymmetric approximation concerns only the derivative $\partial/\partial\theta$, which is zero. For the governing equations that will be solved numerically, the standard parabolic truncation is employed. The continuity equation is therefore given by

$$\frac{\partial\bar{\rho}U}{\partial x} + \frac{1}{r}\frac{\partial r\bar{\rho}V}{\partial r} = 0. \tag{3}$$

The equation for axial momentum, supposing that the positive axial direction is upwards and parallel with the gravitional field, is

$$\frac{\partial\bar{\rho}UU}{\partial x} + \frac{1}{r}\frac{\partial r\bar{\rho}UV}{\partial r} = -\frac{\partial\bar{p}}{\partial x} - \frac{1}{r}\frac{\partial r\bar{\rho}\widetilde{u''v''}}{\partial r} + \bar{\rho}g_x + \text{Mol.Dif.} \tag{4}$$

where g_x is the gravitational acceleration and the

molecular diffusion term is designated by Mol.Dif. When $\partial\bar{p}/\partial x \approx \rho_a g_x$, the buoyancy term is often written as $-(\rho_a-\bar{p})g_x$.

The equation for radial momentum is:

$$\frac{\partial\bar{\rho}UV}{\partial x}+\frac{1}{r}\frac{\partial r\bar{\rho}VV}{\partial r}=-\frac{\partial\bar{p}}{\partial r}-\frac{1}{r}\frac{\partial r\bar{\rho}\widetilde{v''v''}}{\partial r}+\bar{\rho}\frac{\widetilde{w''w''}}{r}+\text{Mol.Dif.} \quad (5)$$

To describe mixing of gases, the mixture fraction F, which signifies the mass fraction of the nozzle fluid, is introduced. It obeys a convection–diffusion equation of the form

$$\frac{\partial\bar{\rho}UF}{\partial x}+\frac{1}{r}\frac{\partial r\bar{\rho}VF}{\partial r}=\frac{1}{r}\frac{\partial r\bar{\rho}\widetilde{v''f''}}{\partial r}+\text{Mol.Dif.} \quad (6)$$

The mean density can be obtained from the mean mixture fraction using the equation of state. With constant pressure this leads to

$$\frac{1}{\bar{\rho}}=\frac{F}{\rho_j}+\frac{1-F}{\rho_a} \quad (7)$$

where density fluctuations have been neglected. This is allowed in isothermal jets because the instantaneous density, for which equation (7) is exact, is approximately a linear function of the instantaneous mixture fraction. For a flame this is not true and a probability density function (pdf) of the mixture fraction has to be used to calculate the mean thermochemical variables such as the mean density [11].

2.1. *The second-order model*

It is noted that correlations of the type $\widetilde{u_k''w''}$ are zero when $u_k'' \neq w''$, due to axisymmetry. Thus, the important Reynolds stress equations are those for $\widetilde{u''u''}$, $\widetilde{v''v''}$, $\widetilde{w''w''}$, and $\widetilde{u''v''}$. The equations are written as

$$\frac{\partial}{\partial x_k}(\bar{\rho}U_k\widetilde{u_i''u_j''})=P_{ij}+G_{ij}+D_{ij}+\overline{p'\left(\frac{\partial u_j''}{\partial x_i}+\frac{\partial u_i''}{\partial x_j}\right)}-\frac{2}{3}\delta_{ij}\bar{\rho}\varepsilon \quad (8)$$

in which local isotropy on the smallest scale has been assumed. The first term on the right-hand side is the production term due to mean strain

$$P_{ij}=-\bar{\rho}\left(\widetilde{u_i''u_k''}\frac{\partial U_j}{\partial x_k}+\widetilde{u_j''u_k''}\frac{\partial U_i}{\partial x_k}\right) \quad (9)$$

while the second term is the production due to buoyancy effects

$$G_{ij}=-\bar{\rho}\beta_e\left(g_i\widetilde{u_j''f''}+g_j\widetilde{u_i''f''}\right). \quad (10)$$

The volumetric expansion coefficient β_e is defined as

$$\beta_e=-\frac{1}{\rho}\left(\frac{\partial\rho}{\partial f}\right)_p. \quad (11)$$

The diffusion term is modelled as

$$D_{ij}=C_S\frac{\partial}{\partial x_k}\left[\left(\bar{\rho}\frac{k}{\varepsilon}\widetilde{u_k''u_l''}+\bar{\rho}\delta_{kl}v\right)\frac{\partial\widetilde{u_i''u_j''}}{\partial x_l}\right]. \quad (12)$$

where v is supposed to be constant. The pressure–strain correlation is

$$\overline{p'\left(\frac{\partial u_i''}{\partial x_j}+\frac{\partial u_j''}{\partial x_i}\right)}=\phi_{ij,1}+\phi_{ij,2}+\phi_{ij,3}. \quad (13)$$

Modelling of this term is performed in the literature in two main ways. The first one is called the Launder–Reece–Rodi (LRR) model [12] and is used in the present study. The other important model is due to Lumley [13], who introduced non-dimensional groups consisting of the anisotropy tensor and its principal invariants and the turbulence Reynolds number $Re_t=k^2/(\varepsilon v)$. Then, the pressure–strain correlation is modelled with these variables as parameters.

The 'return to isotropy' term $\phi_{ij,1}$ is expressed in the anisotropy tensor b_{ij} which is defined as

$$b_{ij}=\frac{\widetilde{u_i''u_j''}}{2k}-\frac{1}{3}\delta_{ij}. \quad (14)$$

Here, k is the turbulent kinetic energy per unit mass

$$k=\tfrac{1}{2}\widetilde{u_i''u_i''} \quad (15)$$

using the summation convention. The return term thus becomes

$$\phi_{ij,1}=-C_1\bar{\rho}\varepsilon 2b_{ij}. \quad (16)$$

The constant C_1 is supposed to be independent of Re and Re_t when these are high enough. The mean strain, also called the 'rapid term', is modelled as

$$\phi_{ij,2}=-\alpha(P_{ij}-\tfrac{2}{3}\delta_{ij}P) \quad (17)$$

where the production P of turbulent kinetic energy is

$$P=\tfrac{1}{2}P_{kk}. \quad (18)$$

The buoyancy term in the pressure–strain correlation is modelled as [14]

$$\phi_{ij,3}=-C_3(G_{ij}-\tfrac{2}{3}\delta_{ij}G) \quad (19)$$

with G defined, analogously to P, as

$$G=\tfrac{1}{2}G_{kk}=-\bar{\rho}\beta_e g_k\widetilde{u_k''f''}. \quad (20)$$

The dissipation rate equation is exactly the same as in

the standard k–ε model (see below), except for the diffusion term, which in the Reynolds stress model is the same as in equation (12) with a coefficient $C_{\varepsilon,s}$ instead of C_s.

The scalar turbulence equations are given by [15]

$$\frac{\partial}{\partial x_k}(\bar{\rho}U_k\widetilde{u_i''f''}) = P_i + G_i + D_i + \overline{p'\frac{\partial f''}{\partial x_i}} \tag{21}$$

with shear production defined as

$$P_i = -\bar{\rho}\left(\widetilde{u_k''f''}\frac{\partial U_i}{\partial x_k} + \widetilde{u_i''u_k''}\frac{\partial F}{\partial x_k}\right) \tag{22}$$

and buoyancy production as

$$G_i = -\bar{\rho}\beta_e \boldsymbol{g}_i \widetilde{f''^2}. \tag{23}$$

The diffusion term is modelled as

$$D_i = C_{sf}\frac{\partial}{\partial x_k}\left(\bar{\rho}\frac{k}{\varepsilon}\widetilde{u_k''u_l''}\frac{\partial\widetilde{u_i''f''}}{\partial x_l}\right) \tag{24}$$

The pressure–scalar gradient correlation is defined by

$$\overline{p'\frac{\partial f''}{\partial x_i}} = \phi_{i,1} + \phi_{i,2} + \phi_{i,3} \tag{25}$$

in which the return term is modelled as [15]

$$\phi_{i,1} = -C_{1f}\bar{\rho}\frac{\varepsilon}{k}\widetilde{u_i''f''} - C'_{1f}\bar{\rho}\frac{\varepsilon}{k}b_{ik}\widetilde{u_k''f''}. \tag{26}$$

The mean strain or rapid term is modelled as [15]

$$\phi_{i,2} = 0.8\bar{\rho}\widetilde{u_k''f''}\frac{\partial U_i}{\partial x_k} - 0.2\bar{\rho}\widetilde{u_k''f''}\frac{\partial U_k}{\partial x_i} \tag{27}$$

and the buoyancy term as

$$\phi_{i,3} = -C_{3f}G_i = C_{3f}\bar{\rho}\beta_e \boldsymbol{g}_i \widetilde{f''^2}. \tag{28}$$

From the foregoing we can deduce the parabolized set of equations in cylindrical coordinates where the generalized equation is

$$\frac{\partial}{\partial X}(\bar{\rho}U\tilde{\phi}) + \frac{1}{r}\frac{\partial}{\partial r}(r\bar{\rho}V\tilde{\phi}) = \frac{1}{r}\frac{\partial}{\partial r}\left(r\bar{\rho}D\frac{\partial\tilde{\phi}}{\partial r}\right) + S_\phi \tag{29}$$

with S_ϕ given in Table 1, $P = -\bar{\rho}\widetilde{u''v''}\,\partial U/\partial r$ and $G = -\bar{\rho}\beta_e\,\boldsymbol{g}_x\widetilde{u''f''}$. The scalar dissipation rate ε_f is modelled assuming proportional scales for velocity and scalar turbulence with a time scale ratio of two [16], as

$$\varepsilon_f = 2\widetilde{f''^2}\frac{\varepsilon}{k}. \tag{30}$$

The model constants used in the present study are given in Table 2.

A large collection of available models for the return term and the rapid term is given in the Appendix of the paper of Hytopoulos and Simpson [19].

2.2. *The first-order* (k–ε) *model*

In the k–ε model [20], the Reynolds stresses are expressed in terms of the local strain rate:

$$-\bar{\rho}\widetilde{u_i''u_j''} = \bar{\rho}(\nu_t+\nu)\left(\frac{\partial\tilde{u}_i}{\partial x_j} + \frac{\partial\tilde{u}_j}{\partial x_i}\right) - \frac{2}{3}\delta_{ij}\left(\bar{\rho}k + \bar{\rho}(\nu_t+\nu)\frac{\partial\tilde{u}_l}{\partial x_l}\right) \tag{31}$$

with

$$\nu_t = C_\mu\frac{k^2}{\varepsilon} \tag{32}$$

The scalar flux in equation (6) is approximated with a gradient transport assumption

$$\widetilde{u_i''f''} = -\frac{\nu_t}{\sigma_f}\frac{\partial\tilde{F}}{\partial x_i} \tag{33}$$

and the buoyancy production term G of equation (20) becomes, after using the transport hypothesis, $G = \boldsymbol{g}_x\nu_t\partial\bar{\rho}/\partial f\,\partial F/\partial x$.

In Table 3, P_{f^2} is $2\bar{\rho}\,\partial F/\partial r\,\partial F/\partial r$ and the scalar dissipation rate is modelled with equation (30). The model constants used in the present study are given in Table 4 [20].

3. NUMERICAL METHOD

The governing equations are solved using a parabolized marching algorithm which resembles the (elliptic) TEACH code [21]. The computations are performed by using the continuity equation to obtain the radial velocity V. Using the radial momentum equation for V and solving a pressure correction equation in the radial direction did not show any difference with the use of only the continuity equation. All variables except the radial velocity, the shear stress and the radial scalar flux are located on the same gridpoints which are distributed in an equidistant manner. The gridpoints for the radial velocity and the shear stress are located in between the gridpoints for the other variables. No transformation of the radial distance is employed; this means that the grid expands in the radial direction to allow the jet to expand. Note that this formulation is different from the parabolic algorithm of Patankar and Spalding [22], which is more often used in this type of parabolic computations. 60 gridpoints in the radial direction and an axial forward step size of 0.01 times the local jet half width are used. This was sufficient to obtain a grid independent numerical solution; the 60 gridpoints are also considered sufficient to obtain an accurate solution close to the nozzle. Note that the step size of 0.01 is much smaller than the value of 0.05 reported in el Baz *et al.* [17], the smaller value in the present study

Table 1. Source terms for the second-order model in the generalized equation (29). The 'turbulent diffusion' coefficient D is $C_{\text{diff}}\, k/\varepsilon\, \widetilde{v''v''}$. For all Reynolds stresses, $C_{\text{diff}} = C_s$, for the scalar fluxes and the scalar variance, $C_{\text{diff}} = C_{sf}$, and for the dissipation rate, $C_{\text{diff}} = C_{\varepsilon s}$

Variable	S_ϕ
$\widetilde{u''u''}$	$-2(1-\alpha)\bar{\rho}\widetilde{u''v''}\dfrac{\partial U}{\partial r} - \dfrac{2}{3}\bar{\rho}\varepsilon - C_1\bar{\rho}\dfrac{\varepsilon}{k}(\widetilde{u''u''} - \frac{2}{3}k) + \frac{2}{3}\alpha P$ $-(2-\frac{4}{3}C_3)\bar{\rho}\beta_e g_x \widetilde{u''f''}$
$\widetilde{v''v''}$	$-\frac{2}{3}\bar{\rho}\varepsilon - C_1\bar{\rho}\dfrac{\varepsilon}{k}(\widetilde{v''v''} - \frac{2}{3}k) + \frac{2}{3}\alpha P - \dfrac{2C_s}{r^2}\dfrac{k}{\varepsilon}\bar{\rho}\widetilde{w''w''}(\widetilde{v''v''} - \widetilde{w''w''})$ $-\frac{2}{3}C_3\rho\beta_e g_x \widetilde{u''f''}$
$\widetilde{w''w''}$	$-\frac{2}{3}\bar{\rho}\varepsilon - C_1\bar{\rho}\dfrac{\varepsilon}{k}(\widetilde{w''w''} - \frac{2}{3}k) + \frac{2}{3}\alpha P + \dfrac{2C_s}{r^2}\dfrac{k}{\varepsilon}\bar{\rho}\widetilde{w''w''}(\widetilde{v''v''} - \widetilde{w''w''})$ $-\frac{2}{3}C_3\bar{\rho}\beta_e g_x \widetilde{u''f''}$
$\widetilde{u''v''}$	$-(1-\alpha)\bar{\rho}\widetilde{v''v''}\dfrac{\partial U}{\partial r} - C_1\rho\dfrac{\varepsilon}{k}\widetilde{u''v''} - \dfrac{C_s}{r^2}\dfrac{k}{\varepsilon}\bar{\rho}\widetilde{w''w''}\,\widetilde{u''v''}$ $-(1-C_3)\bar{\rho}\beta_e g_x \widetilde{v''f''}$
ε	$\dfrac{\varepsilon}{k}(C_{\varepsilon 1}(P+G) - C_{\varepsilon 2}\bar{\rho}\varepsilon)$
$\widetilde{u''f''}$	$-\bar{\rho}\widetilde{v''f''}\dfrac{\partial U}{\partial r} - \bar{\rho}\widetilde{u''v''}\dfrac{\partial F}{\partial r} - C_{1f}\bar{\rho}\dfrac{\varepsilon}{k}\widetilde{u''f''} - C'_{1f}\bar{\rho}\dfrac{\varepsilon}{k}(\mathbf{b}_{ru}\widetilde{u''f''} + \mathbf{b}_{wr}\widetilde{v''f''})$ $+0.8\bar{\rho}\widetilde{v''f''}\dfrac{\partial U}{\partial r} - (1-C_{3f})\bar{\rho}\beta_e g_x \widetilde{f''^2}$
$\widetilde{v''f''}$	$-\bar{\rho}\widetilde{v''f''}\dfrac{\partial V}{\partial r} - \bar{\rho}\widetilde{v''v''}\dfrac{\partial F}{\partial r} - C_{sf}\bar{\rho}\dfrac{k}{\varepsilon}\dfrac{\widetilde{w''w''}}{r^2}\widetilde{v''f''} - C_{1f}\bar{\rho}\dfrac{\varepsilon}{k}\widetilde{v''f''}$ $-C'_{1f}\bar{\rho}\dfrac{\varepsilon}{k}(b_{ru}\widetilde{u''f''} + b_{rr}\widetilde{v''f''}) - 0.2\bar{\rho}\widetilde{u''f''}\dfrac{\partial U}{\partial r}$
$\widetilde{f''^2}$	$-2\bar{\rho}\widetilde{v''f''}\dfrac{\partial F}{\partial r} - \rho\varepsilon_f$

was necessary due to the explicit evaluation (based on known upstream variables) of the source terms, while el Baz *et al.* evaluate most source terms implicitly.

The boundary conditions at the nozzle, often called initial conditions in parabolic computations, are those for fully developed pipe flow [23]. The radial velocity and the scalar variance are zero at the nozzle and in the ambient. The mixture fraction is one at the nozzle and zero in the ambient. At the radial jet boundary, the values of all quantities are equal to those in the ambient. For the turbulence quantities this implies a value of zero or a negligibly small value. The computations are performed up to an axial distance of approximately 300 D. Here, no boundary conditions are prescribed due to the parabolic nature of the flow. Full elliptic calculations would require a prohibitively large grid to simulate such a long flow domain.

For all calculations, except in the simulation of the experimental data of the IMST [9] where the experimental coflow velocity was used in the computations, a very small (numerical) coflow velocity of $U_{\text{cofl}} = 0.01$ m s^{-1} was used to stabilize the compu-

Table 2. Model coefficients in the Reynolds stress models (RSM). The constants for the velocity turbulence in RSM I are from ref. [17] and the constants in the scalar turbulence in model RSM II are from ref. [18] (see ref. [15])

Model	C_1	α	C_3	C_s	$C_{\varepsilon 1}$	$C_{\varepsilon 2}$	$C_{\varepsilon s}$	C_{1f}	C'_{1f}	C_{3f}	C_{sf}
RSM I	1.8	0.6	0.5	0.22	1.44	1.92	0.18	4.7	−4.4	0.33	0.22
RSM II	2.3	0.6	0.5	0.22	1.45	1.90	0.18	5.7	−6.1	0.33	0.22

Table 3. Source terms in the generalized equation (29) for the k–ε model. The turbulent diffusion coefficient D is $\mathscr{D} = \nu_t/\sigma_\phi$ with $\nu_t = C_\mu k^2/\varepsilon$

Variable	S_ϕ
k	$P+G-\bar{\rho}\varepsilon$
ε	$\frac{\varepsilon}{k}(C_{\varepsilon 1}(P+G)-C_{\varepsilon 2}\bar{\rho}\varepsilon)$
$\widetilde{f''^2}$	$P_{f''^2}-\bar{\rho}\varepsilon_f$

Table 4. Model coefficients in the k–ε model. The constants in model I are standard [20]; the constants in model II are adapted for the axisymmetric jet

Model	C_μ	$C_{\varepsilon 1}$	$C_{\varepsilon 2}$	σ_k	σ_ε	σ_f	$\sigma_{f''^2}$
k–ε I	0.09	1.44	1.92	1	1.3	0.7	0.7
k–ε II	0.06	1.44	1.92	1	1.3	0.7	0.7

tations. With zero coflow, a converged solution was difficult to obtain. No turbulence was added to the coflow. Buoyancy terms are only present in calculations where the influence of these terms is investigated.

4. DISCUSSION OF RESULTS

4.1. *Constant density flows*

Profiles across the jet. In Fig. 1(a) the non-dimensionalized axial velocity across the jet in the far field ($x/D > 50$), calculated with the k–ε and the RSM, is compared with the experimental data of Panchapakesan and Lumley (PL1) [24] and Hussein *et al.* (HCG) [25]. Both experimental and numerical data are independent of x/D for these axial distances. The RSM predicts lower velocities near the centreline than the k–ε model, while it predicts higher velocities at the jet edge. Especially near the edge, the RSM compares better to the laser Doppler measurements of HCG, while the k–ε results are in between both sets of measurements.

The axial velocity fluctuation intensity across the jet is shown in Fig. 1(b). Here, again, the RSM results compare most favourably with the measurements of HCG, while the k–ε results are in between the two sets of measurements. It is noted that none of the models predicts the weak local off-axis maxima in the experimental curves.

For the radial velocity fluctuation intensity across the jet, which is shown in Fig. 1(c), the RSM again compares favourably with the measurements of HCG, while the k–ε results are now too high. The high values generated by the k–ε model are not very surprising since it is well known that the k–ε model is not capable of predicting the normal stresses very accurately.

In Fig. 1(d), the profile of the non-dimensionalized dissipation rate $\hat{\varepsilon} = \varepsilon \times L_u/U_c^3$, computed with the two models, is shown across the jet, together with the experimental results. The dissipation rate of HCG, based on the assumption of axisymmetry in the smallest scales, comes closest to the RSM results. The k–ε

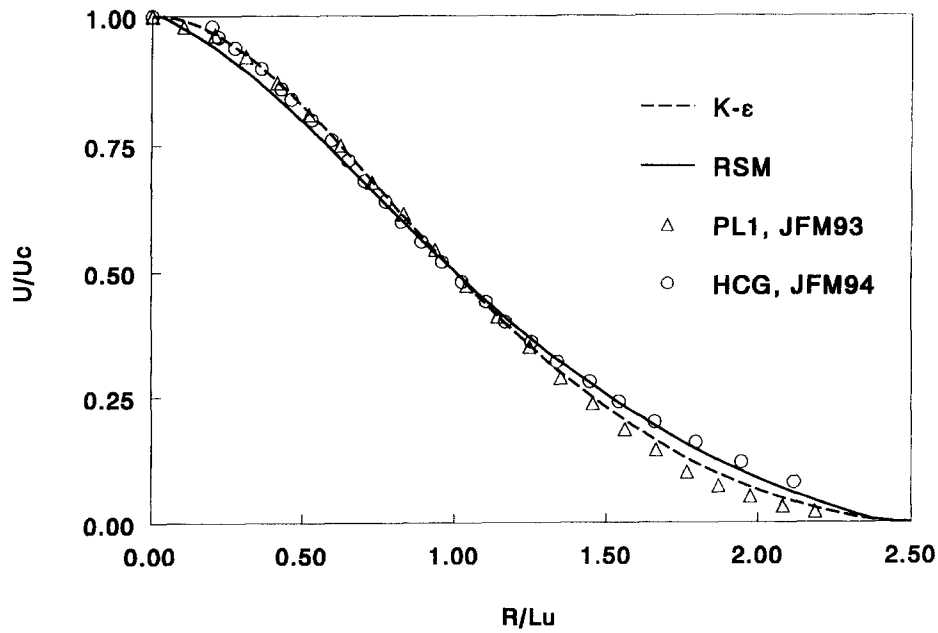

Fig. 1. (a) Far field normalized axial velocity profiles across the jet vs the radial distance normalized by the local jet halfwidth, (b) far field axial velocity fluctuation intensity across the jet vs the radial distance normalized by the local jet halfwidth, (c) far field radial velocity fluctuation intensity across the jet vs the radial distance normalized by the local jet halfwidth, (d) far field normalized dissipation rate $\varepsilon L_u/U_c^3$ across the jet vs the radial distance normalized by the local jet halfwidth. Solid line—RSM, dashed line—k–ε model, triangles—measurements of Panchapakesan and Lumley (PL1) [24], circles—measurements of Hussein *et al.* (HCG) [25].

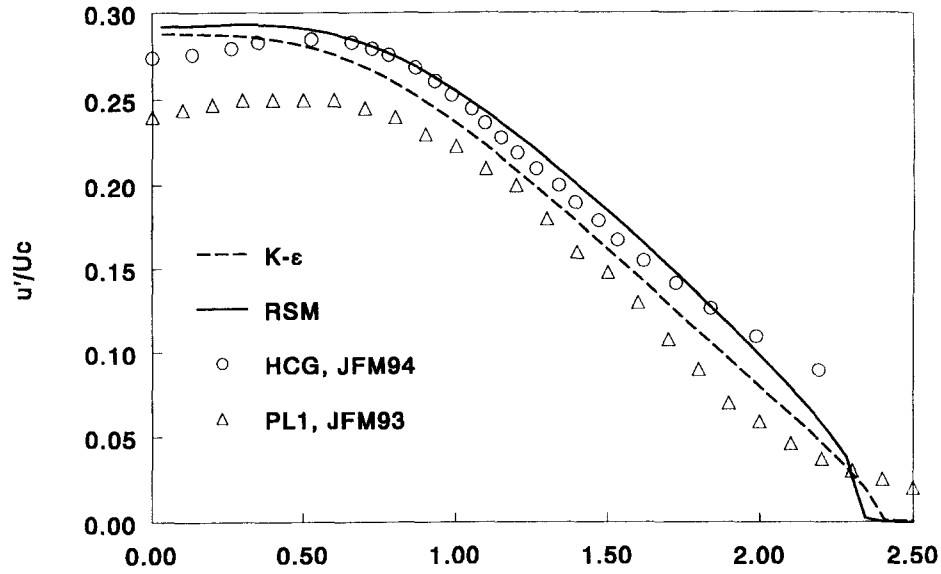

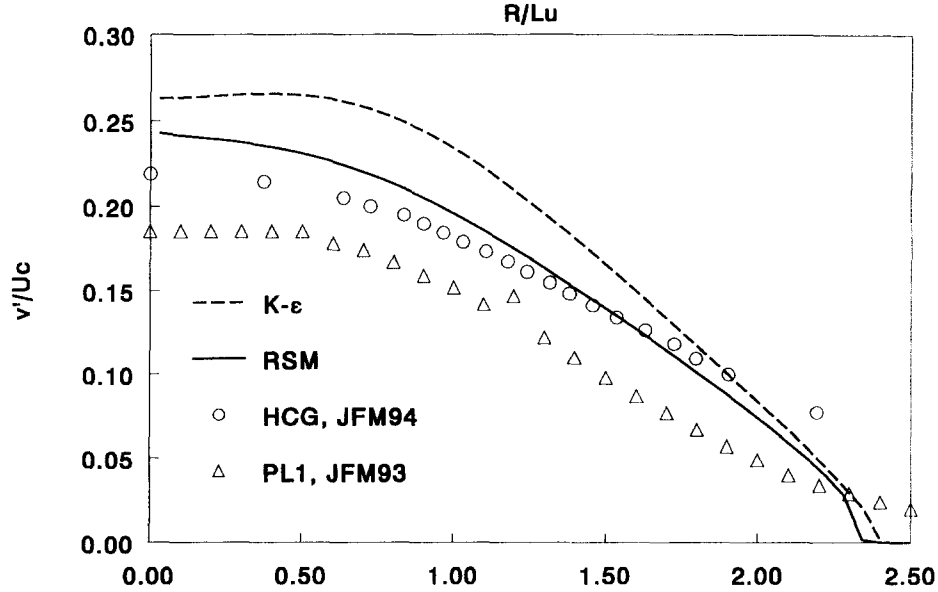

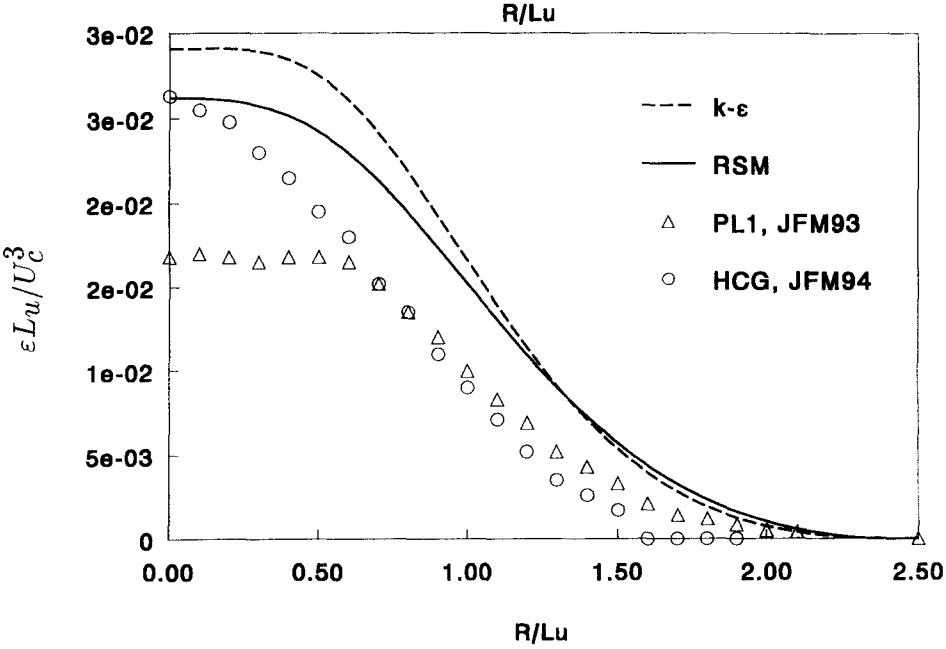

Fig. 1—*continued.*

results are somewhat higher near the centreline, while near the edge all profiles show the same behaviour.

The better performance of the RSM regarding the differences between axial and radial velocity fluctuations (anisotropy) is shown in Figs. 2(a) and (b), where the predicted turbulence intensities on the centreline of an air–air jet are compared with the IMST data. The maxima occur at the location where the axial velocity has the largest gradient in the axial direction, i.e. at the end of the core region. In the near field especially, the predicted difference between the two intensities is too small with the k–ε model (Fig. 2(a)). Concerning the difference between the two fluctuating components, the predictions with the RSM are better (Fig. 2(b)), although the values of the maxima are still too high. This near field behaviour is very much influenced by the initial conditions, but to obtain better agreement changing these conditions as a function of ω would be required [26]; also, part of the discrepancy might be due to the assumption of parabolicity of the flow.

Asymptotic behaviour. In free jets the spreading rates are defined as $S_u = dL_u/dx$ and $S_f = dL_f/dx$, where L_u and L_f are the local halfwidths of the (excess) velocity and mixture fraction, respectively. It is noted that even in constant density flows the mixture fraction and related quantities such as S_f and the turbulent Schmidt number can be computed, although measurements for these quantities are mostly performed for variable density flows only. With the second-order model, and employing a somewhat finer axial stepwidth of 0.005 times the local halfwidth instead of the 0.01 which is used in the rest of the calculations, a spreading rate of 0.1270 is obtained. el Baz *et al.* [17], using exactly the same (second-order) turbulence model, obtained a spreading rate in the axisymmetric jet into stagnant surroundings of 0.1266. In the rest of the paper an axial stepwidth of 0.01 is used. This gives a spreading rate of 0.128, which is a difference of less than 1% with the finer grid and this is considered accurate enough. For the RSM calculations it is noted that the parabolic truncation gives a spreading rate 12.5% larger than when the full elliptic equations are solved [17], the elliptic result (0.113, [17]) still being 15% larger than the latest experimental values of 0.096 [24] and 0.094 [25]. With the k–ε model we obtain a spreading rate of 0.120, which is the value mostly quoted in the numerical literature [27–29].

The rather large difference between the experimental and numerical spreading rates is not considered to be very problematic since we are interested mainly in the influence of density variations on the characteristic properties of jets. The influence of varying density is not considered to be dependent on the precise value of the spreading rate. Moreover, since the characteristic values which are to be computed are mostly dimensionless quantities, non-dimensionalized by typical length and velocity scales such as the axial distance and the local centreline velocity, the exact values of, for instance, the centreline velocity is not material. For the second objective of the present study, i.e. a comparison of the influence of variable density between k–ε and RSM predictions, the exact spreading rate is also of minor importance.

As an intermezzo, a suggestion is given for a change in the coefficients in both models (models II of Tables 2 and 4) to reproduce the experimental spreading rates. In the RSM C_1 has been increased from 1.8 to 2.3 to increase the return to isotropy, and thus to decrease the value of $\widetilde{u''v''}$ which mainly determines the spreading rate. Here, the scalar transport coefficients have been adapted to those of ref. [18]. In the k–ε model only the turbulent viscosity has been diminished ($C_\mu = 0.06$); the fixed turbulent Schmidt number keeps the ratio between S_u and S_f approximately fixed. The characteristic parameters predicted with the models and the experimental data are given in Table 5. The parameters are the spreading rates and centreline quantities such as decay rates for centreline velocity and mixture fraction, K_u and K_f, defined as $U_j/U_c = K_u x/D$ and $1/F_c = K_f x/D$, turbulence intensities

$$\sqrt{k}/U_c, \quad \sqrt{\widetilde{u''u''}}/U_c, \quad \sqrt{\widetilde{v''v''}}/U_c,$$

and unmixedness

$$\sqrt{\widetilde{f''^2}}/F_c.$$

It is seen that these parameters are well predicted with the adapted RSM (RSM II). The k–ε models fail to predict the turbulence anisotropy.

In the following, all computations are performed with the 'classical' coefficients of RSM I and k–ε I, in view of the earlier remarks on the importance of the spreading rate for variable density effects.

4.2. *Variable density flows*

In the calculation of variable density jets, only the jet density ρ_j has been changed to vary ω; all other quantities were kept constant. The choice of keeping the Reynolds number, the Froude number or the momentum flux constant would not change the results. This is because in the equations, there are no Reynolds number dependencies, so the solution is independent of the Reynolds number. The Froude number changes if buoyant jets are considered, but no comparisons between computations at different ω are presented when buoyant jets are considered. Keeping the momentum flux constant in the calculations would not change the results from the present ones because variables normalized by appropriate powers of the exit velocity U_j are invariant with regard to U_j when buoyancy is unimportant. In the computations the centreline velocity in the nozzle was 150 m s^{-1} and the nozzle diameter was 0.01 m.

4.2.1. *Near field behaviour.* In the region near the nozzle exit the density gradients in the flow are the largest. Farther away from the nozzle, mixing with

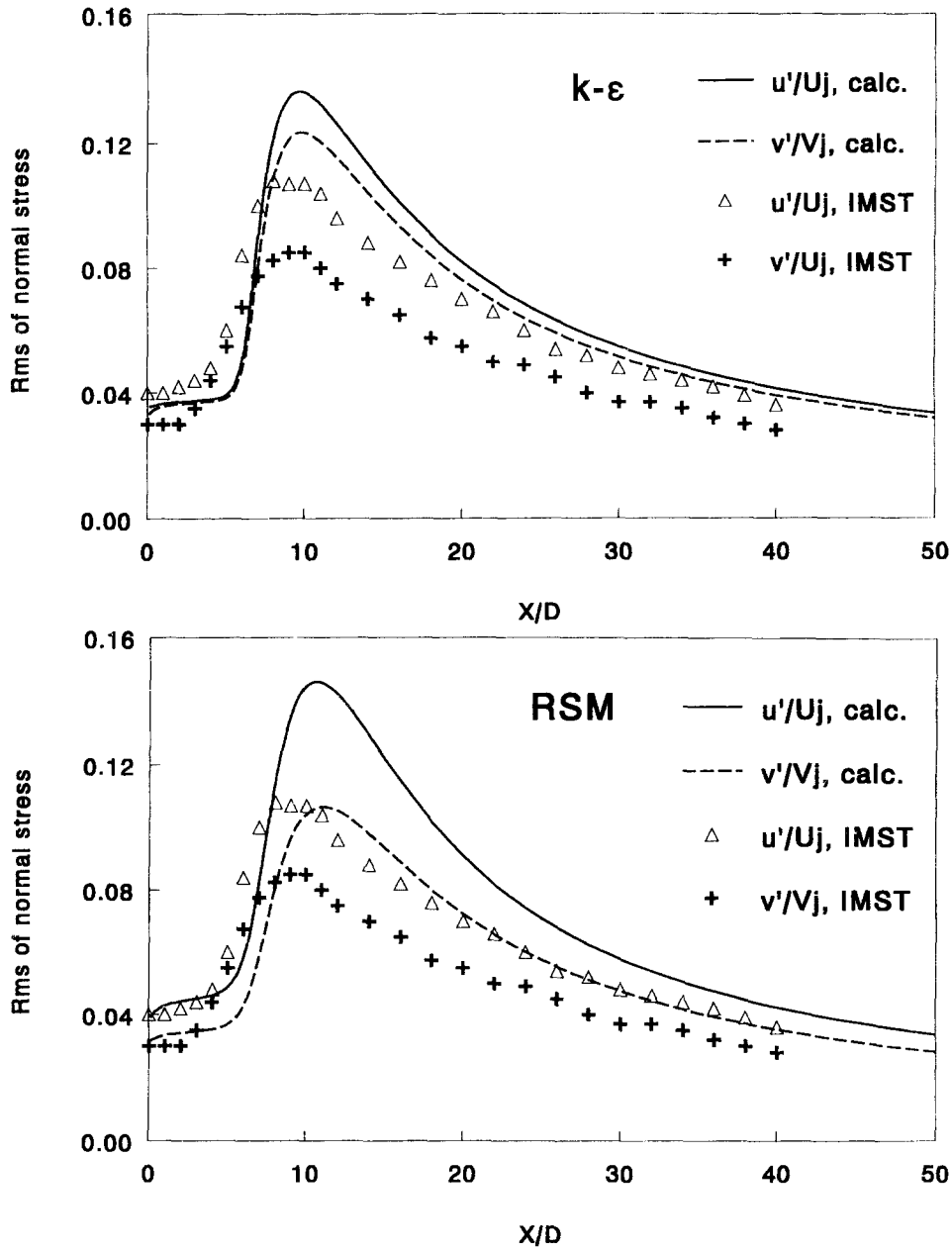

Fig. 2. Root mean square of normalized axial and radial velocity fluctuations on the centreline of the air–air jet: (a) curves are k–ε predictions and symbols are measurements of the IMST [9]; (b) curves are RSM predictions.

Table 5. Predicted and experimental characteristic asymptotic values for axisymmetric jets without density effects. The experiments of ref. [10] ($0.64 < \omega < 7.2$) did not show any effect of ω on the characteristic parameters

	S_u	S_f	K_u	K_f	$\frac{\sqrt{k}}{U_c}$	$\frac{\sqrt{\widetilde{f''^2}}}{F_c}$	$\frac{\sqrt{\widetilde{u''u''}}}{U_c}$	$\frac{\sqrt{\widetilde{v''v''}}}{U_c}$
Exp. [24]	0.096	—	0.165	—	0.25	—	0.24	0.19
Exp. [25]	0.094	—	0.169	—	0.29	—	0.28	0.22
Exp. [10]	—	0.113	—	0.21	—	0.23	—	
RSM I	0.128	0.144	0.218	0.247	0.32	0.24	0.29	0.25
RSM II	0.096	0.114	0.165	0.197	0.28	0.23	0.25	0.22
k–ε I	0.121	0.146	0.205	0.249	0.34	0.25	0.29	0.27
k–ε II	0.098	0.119	0.166	0.200	0.33	0.24	0.28	0.27

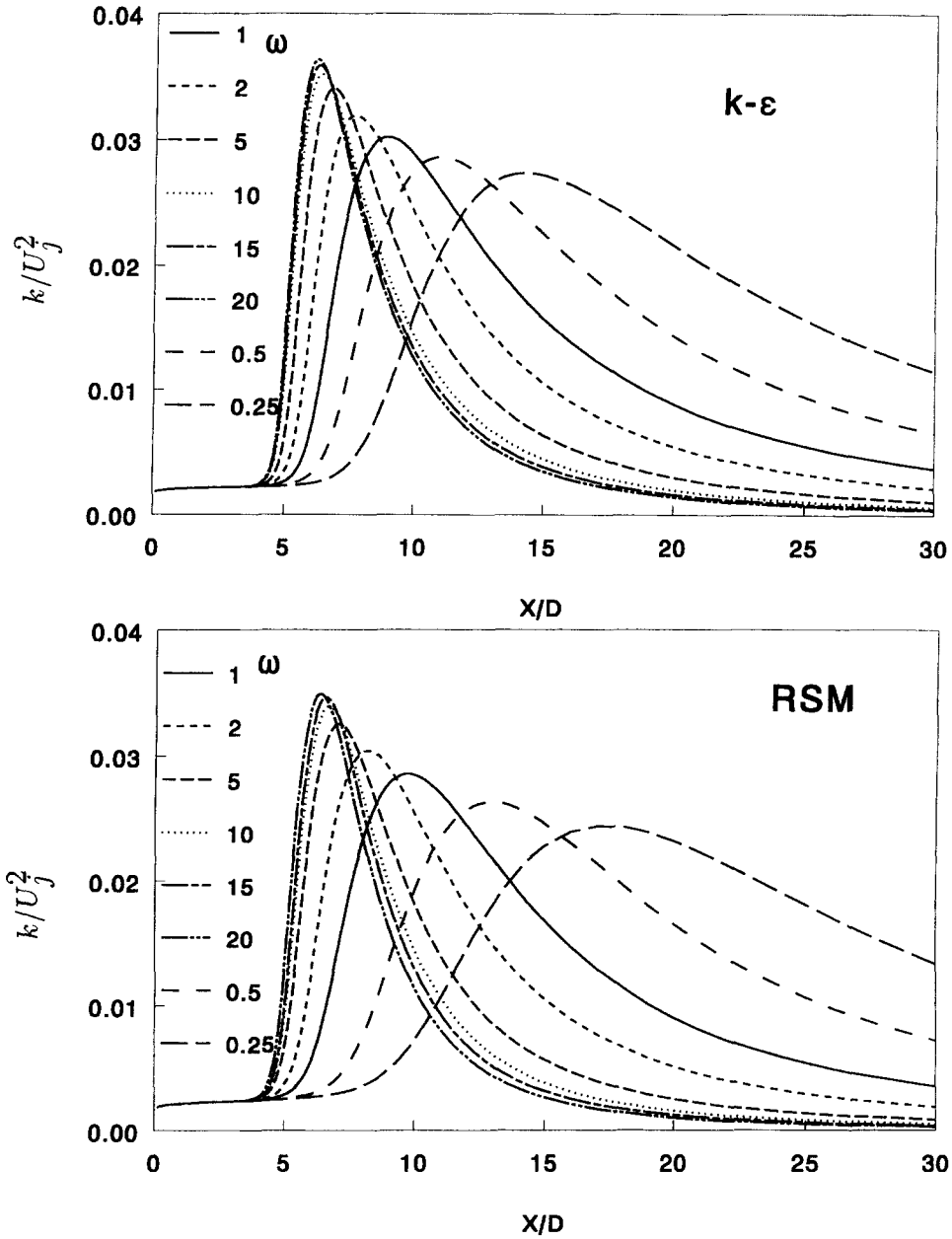

Fig. 3. Centreline values of the normalized turbulent kinetic energy at various density ratios predicted with (a) the k–ε model and (b) the RSM.

ambient air leads to smaller and smaller density gradients until, at even farther distances, the jet is essentially a constant density jet. This is in contrast with, for instance, a flame, in which the density differences are sustained by the chemical reactions and are large until far beyond the flame tip.

In Fig. 3(a) and (b) the effect of the initial density ratio on the centreline turbulent kinetic energy is shown. The lower the jet density ρ_j, the more the maximum turbulence energy shifts towards the nozzle, while the reverse is observed for heavy jets. This is because the maximum turbulence energy occurs approximately at the position where the mean axial centreline velocity begins to drop significantly, i.e. where the core region ends. The core region becomes shorter in light jets due to mixing with heavy ambient air which increases the mean cross-sectional density. Since the axial momentum flux at each jet cross-section is constant, the velocity should decrease faster than in a constant density jet. For heavy jets the reverse holds. From Fig. 3(a) and (b) it can also be observed that there is no qualitative difference between the predictions with the k–ε model and the RSM.

A comparison with the experimental data of IMST for a helium–air jet ($\omega \approx 7.2$) [9] for the axial and radial velocity fluctuation intensities is provided in Fig. 4 for both models. Although both models over-predict the axial distance at which the maxima occur,

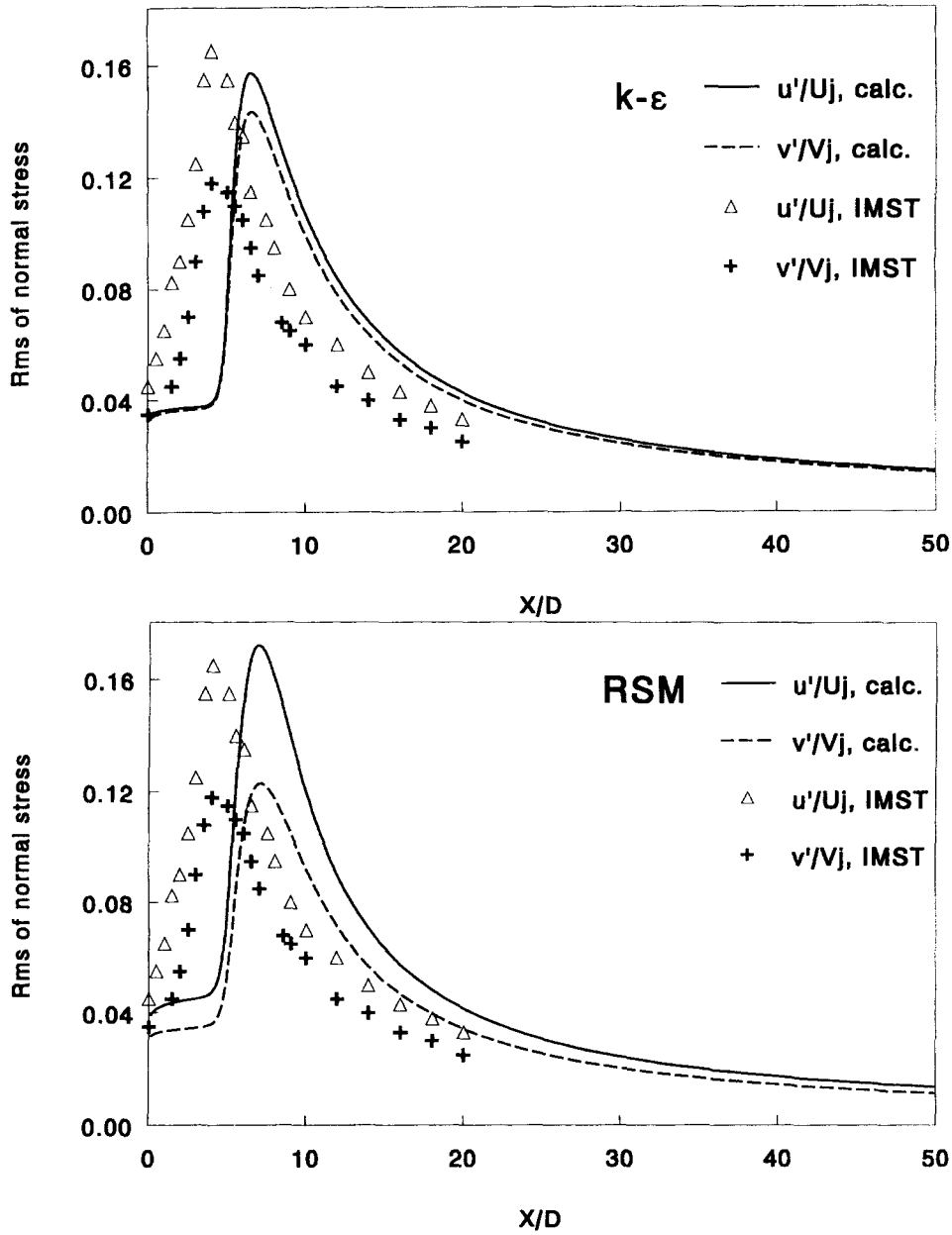

Fig. 4. Root mean square of normalized axial and radial velocity fluctuations on the centreline of the helium–air jet, (a) curves are k–ε and (b) curves are RSM predictions; symbols are measurements of the IMST [9].

the RSM predicts the heights of the curves fairly well. This is in contrast with the k–ε model, which predicts a too small difference between the maximum values of the two intensities, as also observed in the constant density jet (Fig. 2).

4.2.2. *Far field behaviour. Decay rates*. The axial decrease of the mean velocity and mixture fraction is influenced significantly by ω. This is directly related to the mixing of fluids of different density in the early development of the jet (near the nozzle exit). For instance, if a light jet ($\omega > 1$) issues into air, and buoyancy can be neglected, then the velocity will drop faster with axial distance than in a jet with $\omega = 1$. This is due to the conservation of momentum flux at each cross-section of the jet. As heavy surrounding gas is mixed with the lighter jet fluid, the mean cross-section averaged density will become larger with axial distance. Consequently, the velocity must drop faster than in a jet with $\omega = 1$, if momentum is to be conserved; the inverse can be argued for heavy ($\omega < 1$) jets. To capture this influence of entrainment on the axial development of U and F, the decay laws are often written using an effective diameter D_{eff} as

$$\frac{U_j}{U_c} = K_u \frac{x}{D_{\text{eff}}} \quad \text{and} \quad \frac{1}{F_c} = K_f \frac{x}{D_{\text{eff}}} \tag{34}$$

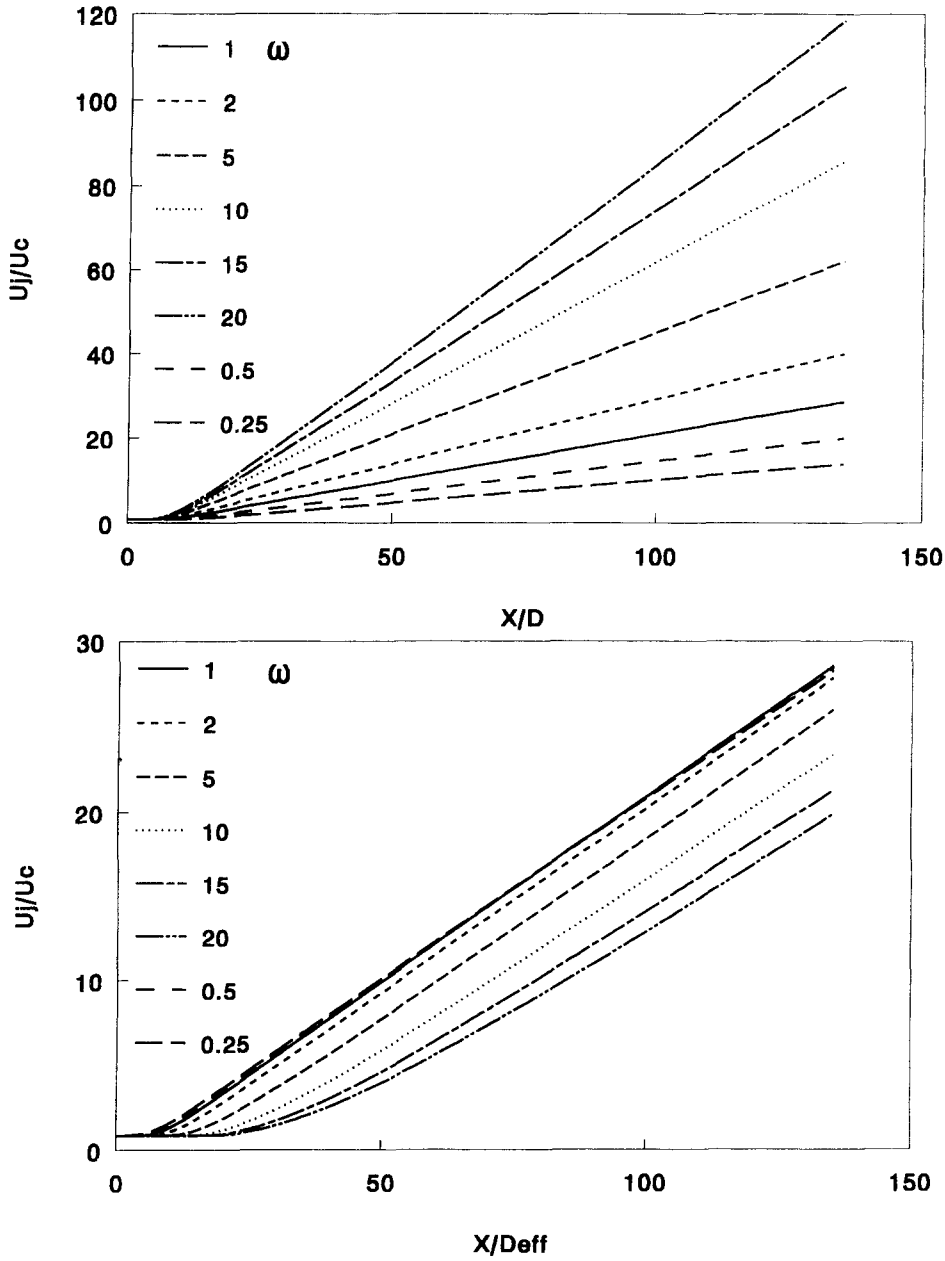

Fig. 5. Velocity decay U_j/U_c on the centreline of variable density jets predicted with the RSM : (a) the axial distance is normalized by the nozzle diameter D and (b) the effective diameter D_{eff} is used.

with $D_{eff} = D\sqrt{\rho_j/\rho_a}$. Using this effective diameter, one hopes to find ω-independent values for K_u and K_f. The physical idea is that the actual (variable density) jet should have the same momentum flux as a constant density jet issuing from a nozzle with $D = D_{eff}$. The behaviour of a jet with $\omega \neq 1$ in which D is replaced with D_{eff} will however be the same as a constant density jet only in the far field where the density across the jet is almost uniform. Indeed, effects of a locally varying density, such as in the near field, will not be captured by the effective diameter concept. In Fig. 5(a), the slope of the inverse centreline velocity is shown to vary significantly using the normal diameter. When the effective diameter is used, all curves have approximately the same slope for all values of ω (Fig. 5(b)). The virtual origins of the curves in Fig. 5(a), defined by the value of x_0/D where the function $U_j/U_c = a + bx/D$ (for $x/D > 50$) is zero, show a decreasing trend with $1/\sqrt{\omega}$. This was also found by Sautet [30]. However, his jet configuration is different from the present one regarding coflow and initial conditions, such that a detailed comparison cannot be made.

In Table 6 the numerical values of the decay rates, normalized by D_{eff}, are given relative to the values at $\omega = 1$. At the light jet side ($\omega > 1$), a slight deviation from the $\omega = 1$ case begins to emerge, while at $\omega = 20$

Table 6. Predicted velocity and scalar decay rates for both models: $K'_u = K_u/K_u(\omega = 1)$ etc. Absolute values for $\omega = 1$: k–ε model 0.205–0.249 and RSM 0.218–0.247. The predicted values are determined from a linear curve-fit between 100 and 300D

ω	k–ε K'_u–K'_f	RSM K'_u–K'_f
1	1.00–1.00	1.00–1.00
2	0.993–0.990	0.995–0.999
5	0.982–0.977	0.987–0.996
10	0.976–0.986	0.978–0.982
15	0.969–0.973	0.972–0.978
20	0.964–0.967	0.967–1.03
0.5	1.007–1.010	0.989–0.967
0.25	1.014–1.017	0.983–0.941

Table 7. Computed velocity and scalar spreading rates for both models. Spreading rates for $\omega \neq 1$ are relative to the value at $\omega = 1$. Absolute values at $\omega = 1$: k–ε model 0.121–0.146 and RSM 0.128–0.144. The predicted values are determined from a linear curve-fit between 200 and 300D

ω	k–ε S_u–S_f	RSM S_u–S_f
1	1.000–1.000	1.000–1.000
2	0.996–0.996	0.999–1.000
5	0.990–0.988	0.989–0.999
10	0.983–0.980	0.982–0.981
15	0.978–0.974	0.977–0.976
20	0.974–0.969	0.973–0.972
0.5	1.002–1.003	1.003–1.003
0.25	1.005–1.005	1.006–1.006

the difference for both models is less than 3.3% which is still considered very small, so no large influence of ω on the normalized decay rates is observed. For K_f this agrees very well with the experiments of Richards and Pitts (RP) [10], while for K_u no conclusive measurements seem to exist. It must be noted that the decay rates in ref. [26] were not completely independent of ω using the given definition of the effective diameter. This could be due to the larger axial distance ($100 < x/F < 300$) used in the present study to determine the decay rates: the larger x/D, the more uniform the density across the jet. Sarh and Gökalp [31] showed that the effective diameter used in the present study works less well for plane jets and that the ambient air density in the expression for the effective diameter should be replaced by the cross-section averaged density. This may be due to the slower axial decay of the mixture fraction ($F \sim x^{-1/2}$ for plane jets) and the resulting slower approach of the cross-section averaged density towards the ambient density.

Experimental data for K_u are 0.165 [24], 0.169 [25] and 0.172 [32] for air–air jets. Pitts in his review on variable density jets [33] gives $K_f = 0.2 \pm 10\%$ (K_f defined using the effective diameter) and Richards and Pitts [10] give $K_f = 0.21$, independent of ω.

It should be added that experimental data on K_u and K_f in jets with strong variable density effects are only useful when the Froude number (Fr) is sufficiently high, otherwise U_j/U_c and $1/F_c$ are not linear functions of x/D. In light jets with buoyancy effects, the velocity decay is slower and the mixture fraction decay is larger than when Fr is very high (see below).

Spreading rates. Calculated values of S_u and S_f with the two models are shown in Table 7 for density ratios $0.25 < \omega < 20$. The primary remark to be made is that there is no significant influence of ω on the spreading rates in both models. At least for the scalar spreading rate this agrees very well with the experimental study of Richards and Pitts [10] who investigated free non-buoyant jets with $0.64 < \omega < 7.2$. In the experimental literature on S_u, it is often reported that the spreading rate increases with ω, i.e. light jets ($\omega > 1$) have larger spreading rates. Panchapakesan and Lumley (PL2) [7] found a spreading rate ($S_u = 0.116$) in a helium–air jet which is 21% larger than in their air–air jet ($S_u = 0.096$), also Wittmer [5] and Streb [6] found larger spreading rates (S_u) in methane and natural gas into air jets ($\omega \approx 1.5$). The differences found numerically for both models (without buoyancy) at these values of ω are less than 2%. On the other hand, Gouldin *et al.* [8] conclude from a review of experimental data that the spreading rates are not influenced by ω, this is also what has been found by Sarh [33] and Sautet [30]. It must be noted that the relative difference between experimental values and predictions for S_u and S_f are the same as those for the spreading rates K_u and K_f, this is due to the intimate linkage between halfwidths and centreline decay in the absence of buoyancy.

It should be noted that the experiments on variable density jets are usually performed in configurations such that buoyancy effects are not negligible when the Froude number is not high enough. The influence of including buoyancy in the present calculations with $\omega > 1$ is, however, not to increase but to decrease the spreading rates, even when buoyancy induced turbulence production is included (see below).

Turbulence intensity. The centreline turbulence intensity $\sqrt{k_c}/U_c$ becomes constant after a certain axial distance, see Fig. 6(a) and (b) for the k–ε and RSM, respectively. The distance required to attain the asymptotic value varies with ω. Light jets reach their asymptotic value earlier than heavy jets. This is confirmed by experiments [8, 9] and other numerical computations [26]. There is again little difference between the behaviour of the first- and second-order models. Some experimental studies indicate higher turbulence intensities in light jets [7, 34, 35] which are attributed to the initial development of the jets in [7, 35]. This is not found in the computations since the models 'forget' the initial development.

Unmixedness. The centreline unmixedness, defined as

$$\sqrt{\widetilde{f''^2_c}}\Big/F_c$$

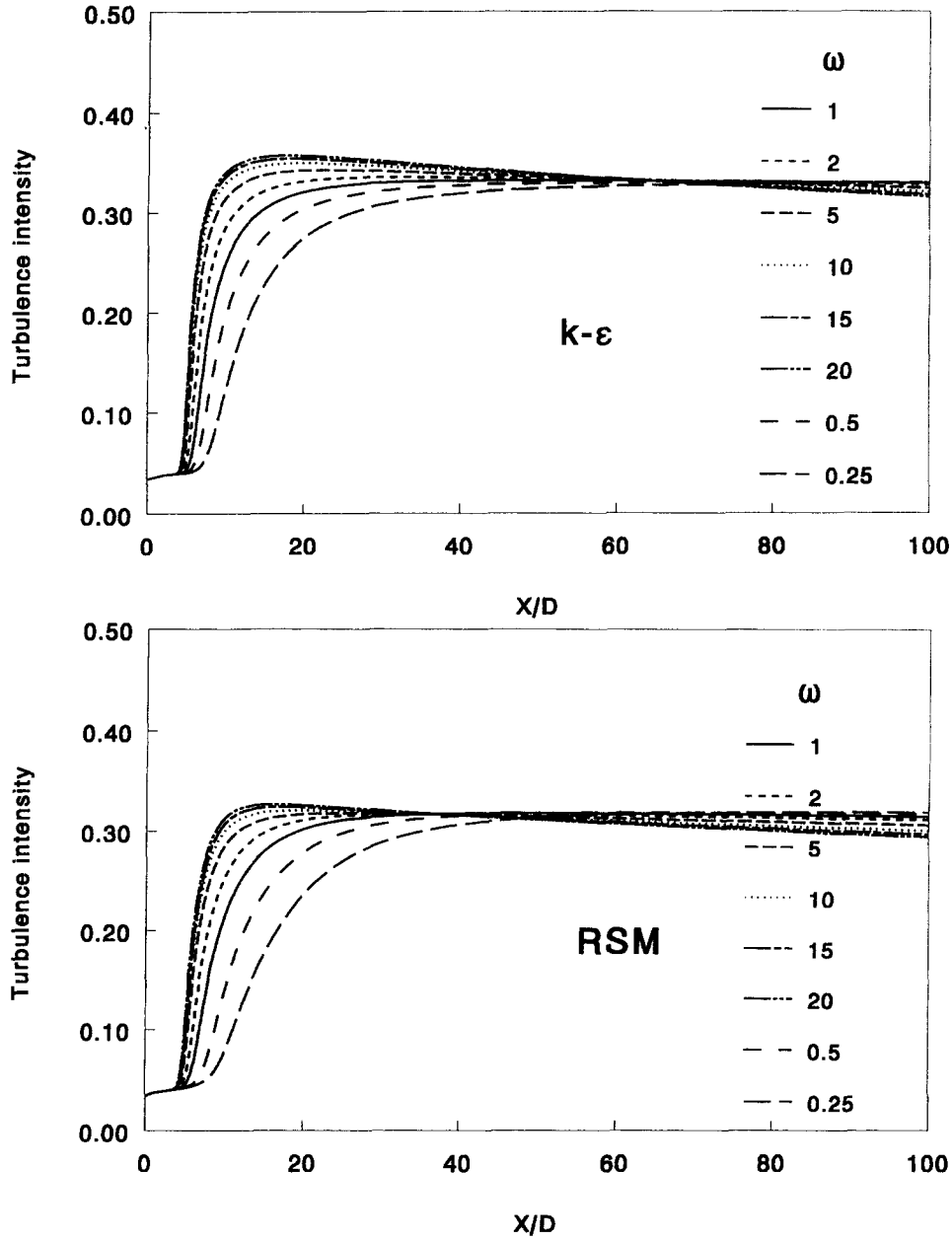

Fig. 6. (a), (b) Turbulence intensity $\sqrt{k}/U_c$ on the centreline of the jets predicted with (a) the k–ε model and (b) with the RSM, (c) and (d) unmixedness $\sqrt{\widetilde{f''^2}}/F_c$ on the centreline of the jets predicted with (c) the k–ε model and (d) with the RSM.

also becomes independent of axial distance and the asymptotic value is independent of ω as well [see Fig. 6(c) and (d)]. These conclusions agree with experimental data [10] and a review of experimental data by Pitts [33]. The RSM predicts a slight peak in the near field before the unmixedness reaches its final value. This behaviour can also be observed in the numerical results of ref. [26]. Again there is very little difference between the first- and second-order models.

Influence of buoyancy. The gravity force in the mean momentum equation increases the cross-section averaged axial momentum flux while there are also buoyancy production terms in the Reynolds stress equations that modify the turbulence structure.

It must be noted that the axial decay laws in jets and plumes are different, e.g. in axisymmetric jets the velocity and mixture fraction decay as x^{-1}, while in plumes the velocity decays more slowly ($x^{-1/3}$) due to the increased momentum flux and the mixture fraction decays faster ($x^{-5/3}$) [1] because of the larger radial velocity gradient and therefore larger turbulent viscosity. Similarity laws are still applicable in plumes.

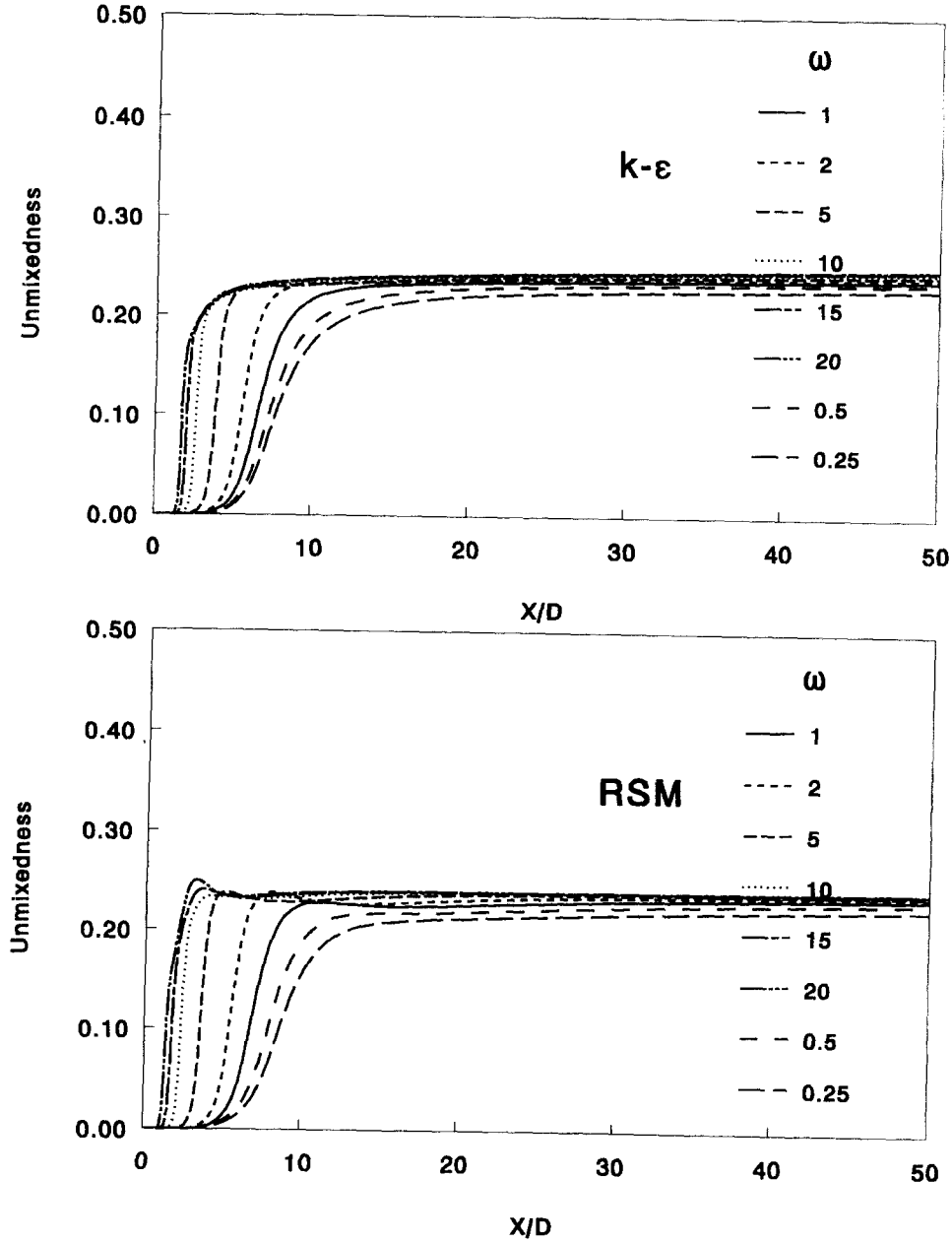

Fig. 6.—*Continued.*

Further, it is important to note that the centreline turbulence intensities

$$\sqrt{\widetilde{u''u''}}/U_c \quad \text{and} \quad \sqrt{\widetilde{v''v''}}/U_c,$$

the unmixedness and the normalized axial scalar flux $\widetilde{u''f''}/(U_cF_c)$ at large x/D are constant, just as in non-buoyant turbulent jets, see for instance ref. [36].

Computations in this section are performed with the RSM, since buoyancy turbulence production cannot be adequately simulated with the k–ε model. However, both models show the same behaviour regarding the mean and turbulence quantities when only the buoyancy term is in the axial momentum equation, but no buoyancy turbulence production is taken into account.

In Fig. 7, the inverse normalized centreline velocity and the inverse mixture fraction are shown for the case of the helium–air jet of PL2 [7] ($Fr = 14 \times 10^3$, $x_b/D \approx 37$). The slower velocity decay and the faster mixture fraction decay with respect to the situation without buoyancy in the far field can be observed. The difference between the computations with and without buoyancy becomes apparent for $x/D > 50$.

The measurements of PL2, conducted from 50 to 100 D, showed that the Reynolds stresses involving the axial velocity fluctuation are higher than in a constant

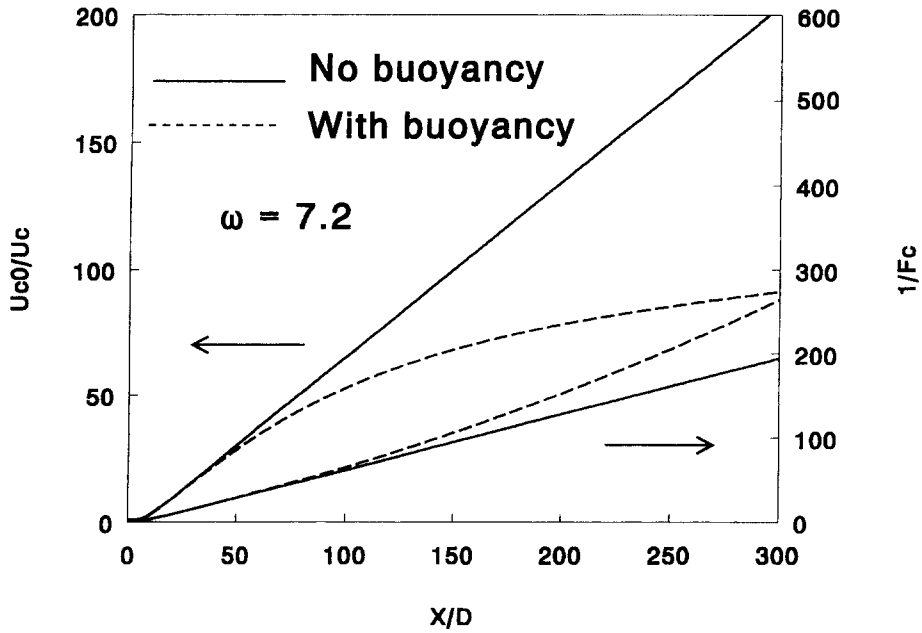

Fig. 7. The inverse normalized centreline velocity U_{c0}/U_c and the inverse mixture fraction $1/F_c$ for the case $\omega = 5$. Solid lines are RSM calculations without buoyancy, dashed lines are calculations with the gravity term in the momentum equation and with turbulence production due to buoyancy.

density jet; this feature is not predicted by the model, see Fig. 8(a). The decreasing trend of the centreline axial turbulence intensity with axial distance, observed by PL2, is correctly predicted. The centreline radial turbulence intensity is measured by PL2 to be of the same order of magnitude as in the constant density jet and this is also what the predictions show (not shown here). Since in the pure jet and pure plume regions the turbulence intensities are independent of axial distance, the decreasing behaviour of these quan-

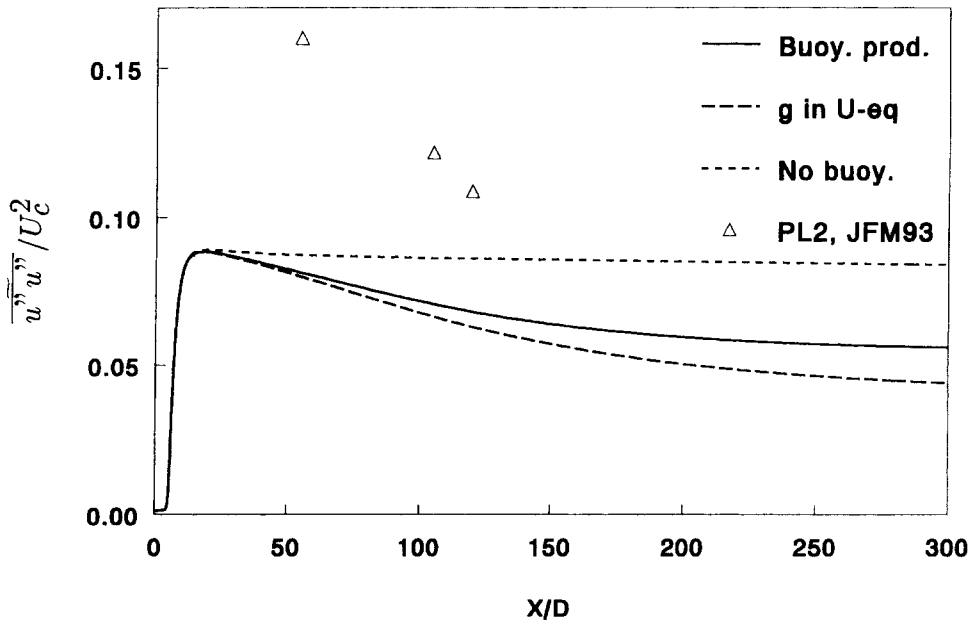

Fig. 8. (a) The influence of buoyancy on the axial turbulence intensity predicted with the RSM, (b) the influence of buoyancy on the centreline axial normalized scalar flux $\widetilde{u''f''}/(U_cF_c)$ with the RSM, and predictions with the k–ε model (dashed-dotted line), (c) the influence of buoyancy on the centreline unmixedness $\sqrt{\widetilde{f''^2}}/F_c$ predicted with the RSM, crosses are experimental data of RP [10], including all buoyancy terms (solid line), including only the buoyancy term in the momentum equation (long dashes) and without buoyancy (short dashes). Symbols are experimental data for the helium jet of PL2.

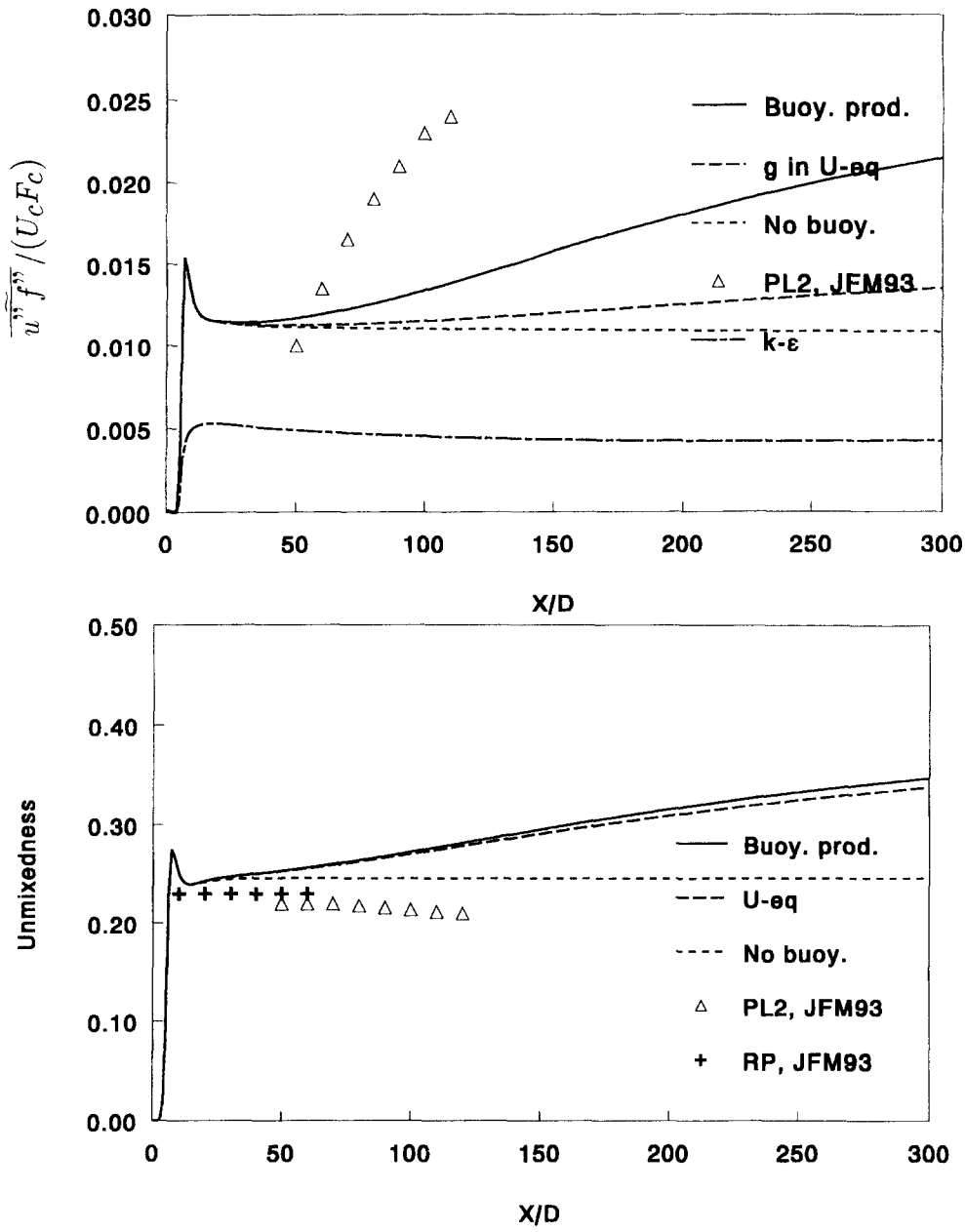

Fig. 8—*continued.*

tities with axial distance indicates that the region of measurement of PL2 is in the intermediate region between the pure jet and pure plume.

PL2 also show that the normalized scalar flux involving the axial velocity fluctuation $\widetilde{u''f''}/(U_cF_c)$ increases with axial distance. This trend is well predicted by the model, although the predicted rate of increase of this normalized flux is lower than in the experiment. The k–ε model does not show any influence of turbulence production due to buoyancy on this flux as can be seen in Fig. 8(b). However, the value of this flux, even in the second-order model, does not exert a large influence on the predictions of all other quantities. According to the measurements of PL2, the normalized radial scalar flux profiles $\widetilde{v''f''}/(U_cF_c)$ show a similar behaviour; this is also reproduced by the predictions (not shown here).

Regarding the influence of buoyancy on the unmixedness, in Fig. 8(c) it can be observed that the gravity term in the axial momentum equation alone already leads to an increasing behaviour in axial direction, while the turbulence production terms lead to an additional slight increase. The experimental data of PL2 for the unmixedness show a constant value (0.21–0.22) between 50 and 100 D which in fact is the same as the value in the predictions without buoyancy. This behaviour is not easily explainable, since the asymptotic unmixedness is 0.23 in a jet and 0.4 in a plume

Table 8. Asymptotic centreline values of turbulence intensities, unmixedness and spreading rates

Quantity	Experimental		RSM		k-ε	
	Jet	Plume	Jet	Plume	Jet	Plume
$\sqrt{\widetilde{u''u''}}/U_c$	0.28 [25]	0.32 [36]	0.29	0.24	0.29	0.20
$\sqrt{\widetilde{v''v''}}/U_c$	0.22 [25]	0.19 [36]	0.25	0.18	0.27	0.19
$\sqrt{\widetilde{f''^2}}/F_c$	0.23 [10]	0.40 [36]	0.24	0.40	0.25	0.42
S_u	0.094 [25]	0.11 [1]	0.127	0.093	0.12	0.091
S_f	0.113 [10]	0.10 [1]	0.144	0.092	0.14	0.088

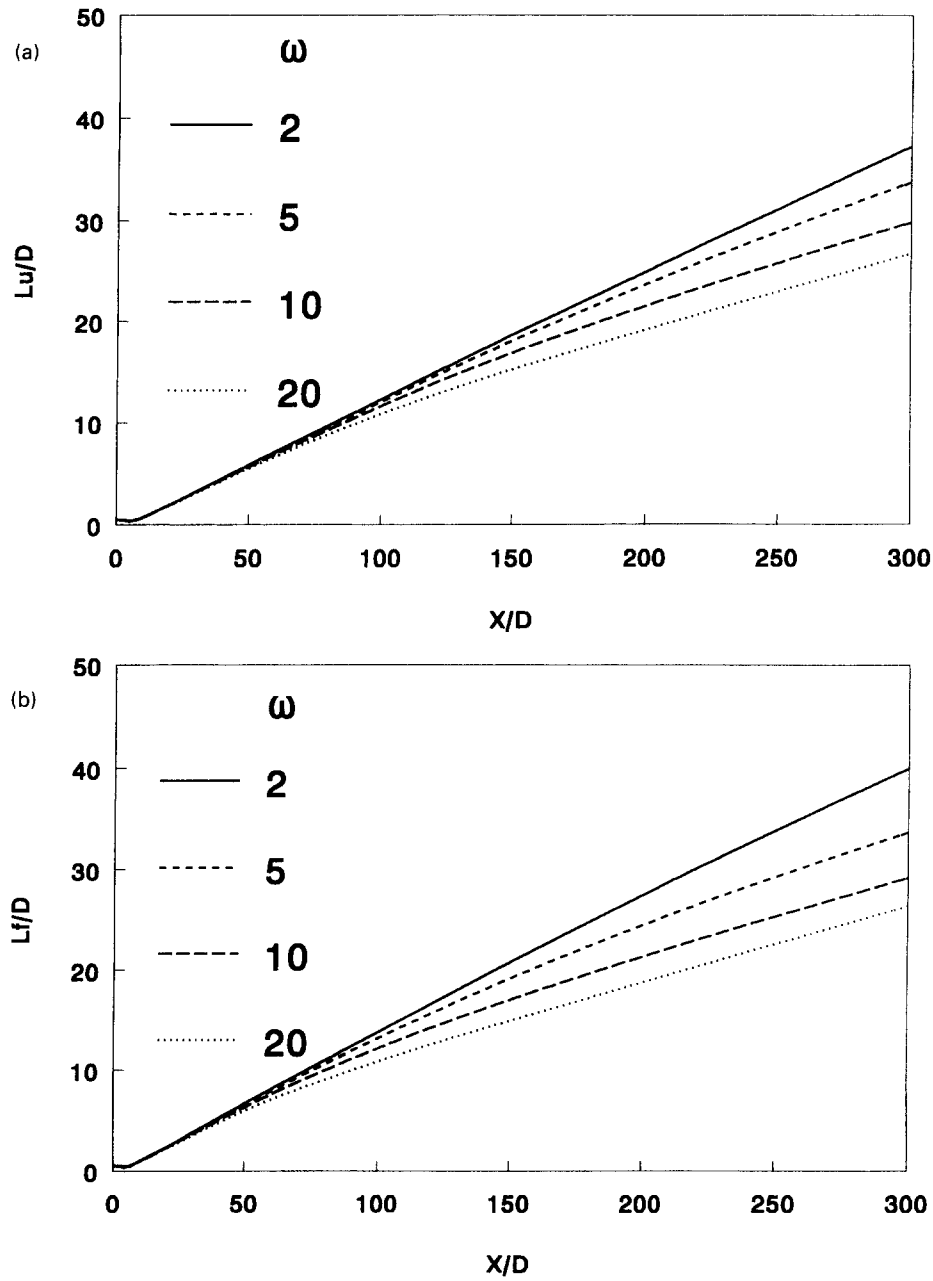

Fig. 9. The influence of the buoyancy term in the momentum equation on (a) the velocity halfwidth L_u and (b) on the scalar halfwidth L_f, predicted with the RSM. Note that, without buoyancy effects ($\omega = 1$), a straight line would be obtained.

[36], see Table 8. The measurement range of PL2 is in the intermediate region between jet and plume, so at least an increase of unmixedness with axial distance would be expected.

With respect to the predictions it must be noted that the k–ε model gives the same behaviour as described above for the RSM, the only difference is that the turbulence production terms due to buoyancy have no influence at all. The reason for the increasing values of unmixedness with x is a larger mixture fraction variance and a smaller mixture fraction on the axis with respect to the case without buoyancy. The smaller mixture fraction is due to the different scaling law in a plume, which has been discussed above.

The decrease of the halfwidths due to buoyancy is illustrated in Fig. 9(a) and (b) where L_u is shown for several values of ω. Here the same boundary conditions have been used as in Table 7 but including the buoyancy term in the momentum equation. The Froude numbers for the cases shown in Fig. 9 are: ($\omega = 2$, $Fr = 153 \times 10^3$, $x_b/D = 164$), ($\omega = 5$, $Fr = 38 \times 10^3$, $x_b/D = 65.4$), ($\omega = 10$, $Fr = 17 \times 10^3$, $x_b/D = 36.8$), ($\omega = 20$, $Fr = 8.1 \times 10^3$, $x_b/D = 21.2$). It must be remarked that the effect of the buoyancy turbulence production terms is to augment somewhat the halfwidths at large values of ω. The decreasing trend of the halfwidths with decreasing Fr and thus increasing influence of gravity can be explained by noting that the gravity force is present most at the interior of the jet where the density in general is lowest for $\omega > 1$. So, the gravitational acceleration in the interior is largest, leading to a narrower velocity profile and thus a smaller spreading rate.

The asymptotic centreline values and spreading rates measured and predicted in the limiting cases of a pure jet and a pure plume are listed in Table 8. Both models give a decrease of the velocity spreading rate from jet to plume, while the experimental data show the opposite behaviour. This indicates a problem with respect to modelling of the buoyancy related turbulence production. For the scalar spreading rate, however, the correct trend is predicted. The experimental data suggest an increase of anisotropy

$$\sqrt{\widetilde{u''u''}} \Big/ \sqrt{\widetilde{v''v''}}$$

in the plume with respect to the jet. This trend is reproduced by the RSM while the k–ε model, as expected, does not show this behaviour. The values of the unmixedness are remarkably well predicted by both the RSM and the k–ε model.

5. CONCLUSIONS

Numerical predictions of variable density axisymmetric turbulent jets have been performed with first- and second-order turbulence models. The RSM results for constant density jets compare well with the numerical study of el Baz *et al.* [17]. The (far field) similarity profiles across the jet predicted with the RSM compare somewhat better with experimental data although the differences with the k–ε model are not very large. The k–ε model fails, especially in the near field, to predict the experimentally observed turbulence anisotropies. For constant density jets, turbulence constants in both models have been adjusted to predict the experimental spreading rates. In particular, the RSM is able to predict all characteristic asymptotic parameters very well.

Without buoyancy, the first- and second-order models show no significant effects of the density ratio ($0.25 < \omega < 20$) on the far field characteristic parameters such as spreading rates, decay rates, turbulence intensity and unmixedness. This is in good agreement with most experimental studies on scalar variables, but regarding velocity spreading rates and the turbulence intensity no real consensus in the experimental literature exists.

Decay rates of velocity and mixture fraction vary with varying ω, but the values are shown to be invariant when the classical effective diameter is used for normalization. In the latter case only differences up to 3% have been observed.

Regarding buoyancy and the effect of turbulence production due to buoyancy, there are large differences between the two models. The buoyancy induced turbulence production terms in the second-order model are essential to reproduce the experimental increase [7] with axial distance of the centreline normalized axial scalar flux in a helium–air jet. The k–ε model does not contain turbulence production terms in the scalar transport equations and consequently fails to predict the trend observed for the axial scalar flux. Finally, a comparison between computations of jets and plumes shows that the trend regarding the velocity spreading rate is wrong in both models, while the trend for the scalar spreading rate is predicted in accordance with measurements. The comparison between asymptotic values of the unmixedness in jets and plumes show that both models predict the correct trend but only the RSM predicts the correct trend for the anisotropy of the turbulence intensities.

Acknowledgement—The French Ministry of Foreign Affairs is acknowledged for a post-doctoral grant to the first author.

REFERENCES

1. C. J. Chen and W. Rodi, *Vertical Turbulent Buoyant Jets, A Review of Experimental Data*. Pergamon Press, Oxford (1980).
2. M. W. Thring and M. P. Newby, Combustion length of enclosed turbulent jet flames, in *4th Symp. on Combustion* the Combustion Institute, pp. 789–796, Pittsburgh, PA (1952).
3. P. Chassaing, G. Harran and L. Joly, Density fluctuation correlations in free turbulent binary mixing, *J. Fluid Mech.* **279,** 239–278 (1994).
4. H. Ha Minh, B. E. Launder and J. MacInnes, The turbulence modelling of variable density flows—a mixed-weighted decomposition, in *Turbulent Shear Flows* 3, pp. 291–308. Springer, Berlin (1981).

5. V. Wittmer, Geschwindigkeit und Temperatur in einer turbulenten Freistrahldiffusionsflamme. Ph.D. Thesis, Universität Karlsruhe, Karlsruhe (1980).
6. H. Streb, Untersuchungen zum Einfluss des Auftriebs auf die Mischung und Reaktion in turbulenten Freistrahldiffusionsflammen. Ph.D. Thesis, Universität Karlsruhe, Karlsruhe (1993).
7. N. R. Panchapakesan and J. L. Lumley, Turbulence measurements in axisymmetric jets of air and helium. Part 2. Helium jet. *J. Fluid Mech.* **246,** 225–247 (1993).
8. F. C. Gouldin, R. W. Schefer, S. C. Johnson and W. Kollmann, Nonreacting turbulent mixing flows, *Prog. Energy Combust. Sci.* **12,** 257–303 (1986).
9. T. Djeridane, F. Anselmet, M. Amielh and L. Fulachier, Experimental investigation of the near-field region of variable density turbulent jets, In *Proceedings of the Int. Symp. on Refined Flow Modelling and Turbulence Measurements*, pp. 505–512 (1993).
10. C. D. Richards and W. M. Pitts, Global density effects on the self-preservation of turbulent free jets, *J. Fluid Mech.* **254,** 417–435 (1993).
11. J. P. H. Sanders and A. P. G. G. Lamers, Modeling and calculation of turbulent lifted diffusion flames, *Combust. Flame* **96,** 22–33 (1994).
12. B. E. Launder, G. J. Reece and W. Rodi, Progress in the development of a Reynolds-stress turbulence closure, *J. Fluid Mech.* **68,** 537–566 (1975).
13. J. L. Lumley, Computational modeling of turbulent flows, *Adv. Appl. Mech.* **18,** 123–175 (1978).
14. B. E. Launder, On the effect of a gravitational field on the turbulent transport of heat and momentum, *J. Fluid Mech.* **67,** 569–581 (1975).
15. R. Schiestel, *Modélisation et simulation des écoulements turbulents*. Hermes, Paris (1993).
16. C. Beguier, I. Dekeyser and B. E. Launder, Ratio of scalar and velocity dissipation time scales in shear flow turbulence, *Phys. Fluids* **21,** 307–3109 (1978).
17. A. el Baz, T. J. Craft, N. Z. Ince and B. E. Launder, On the adequacy of the thin-shear-flow equations for computing turbulent jets in stagnant surroundings, *Int. J. Heat and Fluid Flow* **14,** 165–169 (1993).
18. M. M. Gibson and B. E. Launder, Ground effects on pressure fluctuations in the atmospheric boundary layer, *J. Fluid Mech.* **86,** 491–511 (1978).
19. E. Hytopoulos and R. L. Simpson, Critical evaluation of recent second-order closure models. AIAA paper 93-0081 (1993).
20. B. E. Launder and D. B. Spalding, The numerical computation of turbulent flow, *Comp. Meth. Appl. Mech. Eng.* **3,** 269–289 (1974).
21. A. D. Gosman and W. M. Pun, Engineering report HTS 73/2, Imperial College Mech. London (1973).
22. S. V. Patankar and D. B. Spalding, *Heat and Mass Transfer in Boundary Layers*. Intertext, London (1970).
23. J. Laufer, NACA report Vol. 1174 (1953).
24. N. R. Panchapakesan and J. L. Lumley, Turbulence measurements in axisymmetric jets of air and helium. Part 1. Air jet, *J. Fluid Mech.* **246,** 197–223 (1993).
25. H. J. Hussein, S. P. Capp and W. K. George, Velocity measurements in a high-Reynolds-number, momentum-conserving, axisymmetric, turbulent jet, *J. Fluid Mech.* **258,** 31–75 (1994).
26. E. Ruffin, R. Schiestel, F. Anselmet, M. Amielh and L. Fulachier, Investigation of characteristic scales in variable density turbulent jets using a second-order model, *Phys. Fluids* **6,** 2785–2799 (1994).
27. S. J. Kline, M. V. Morkovin, G. Sovran, D. J. Cockrell, Computation of turbulent boundary layers, *Proceedings of AFOSR-IFP-Stanford Conference*, Mechanical Engineering Department, Stanford University (1969).
28. D. B. Taulbee, Engineering turbulence models, in *Advances in Turbulence* (Edited by W. K. George and R. Arndt), pp. 75–125. Springer, Berlin (1989).
29. J. P. H. Sanders, Scalar transport and flamelet modelling in turbulent jet diffusion flames. Ph.D. Thesis, Eindhoven University of Technology, Eindhoven (1994).
30. J. C. Sautet, Effets des differences de densites sur le developpement scalaire et dynamique des jets turbulents. Ph.D. Thesis, L'Université de Rouen, Rouen (1992).
31. B. Sarh and I. Gökalp, Variable density effects on the mixing of turbulent rectangular jets, *Proceedings of the Eighth Symp. on Turbulent Shear Flows*. Technical University of Munich, pp. 641–646, (1991).
32. I. Wygnanski and H. Fiedler, Some measurements in the self-preserving jet, *J. Fluid Mech.* **38,** 577–612 (1969).
33. W. M. Pitts, Effects of global density ratio on the centerline mixing behavior of axisymmetric turbulent jets, *Exp. Fluids* **11,** 125–134 (1991).
34. B. Sarh, Contribution a l'étude des jets turbulents a masse volumique variable et des flammes turbulentes de diffusion. Ph.d. Thesis, Université Pierre et Marie Curie, Paris (1990).
35. D. M. Kyle and K. R. Sreenivasan, The instability and breakdown of a round variable-density jet, *J. Fluid Mech.* **249,** 619–664 (1993).
36. A. Shabbir and W. K. George, Experiments on a round turbulent buoyant plume, *J. Fluid Mech.* **275,** 1–32 (1994).